Structure and physical properties of YbZn$_2$Sb$_2$ and YbCd$_2$Sb$_2$

Oksana Ya. ZELINSKA[1,2], Andriy V. TKACHUK[1], Andrew P. GROSVENOR[1], Arthur MAR[1]*

[1] *Department of Chemistry, University of Alberta, Edmonton, Alberta, Canada T6G 2G2*
[2] *Department of Inorganic Chemistry, Ivan Franko National University of Lviv, 79005 Lviv, Ukraine*
* *Corresponding author. Fax: +1 780 492 8231; e-mail: arthur.mar@ualberta.ca*

The ternary ytterbium transition-metal antimonides YbM_2Sb$_2$ (M = Zn, Cd) were confirmed by single-crystal X-ray diffraction studies to adopt the CaAl$_2$Si$_2$-type structure ($P\bar{3}m1$; a = 4.4424(6) Å, c = 7.4184(9) Å for YbZn$_2$Sb$_2$; a = 4.6512(7) Å, c = 7.5661(11) Å for YbCd$_2$Sb$_2$). Electrical resistivity measurements on single crystals revealed weakly metallic behaviour, with a resistivity minimum near 80 K in the case of YbCd$_2$Sb$_2$. The Yb atoms are predominantly divalent, as indicated by band structure calculations and X-ray photoelectron spectroscopy on YbZn$_2$Sb$_2$, but nonzero magnetic moments derived from magnetic susceptibility measurements and additional features in the experimental valence band spectrum provide evidence for the presence of some trivalent Yb species.

Antimonide / Ytterbium / Electronic structure / Magnetic properties

Introduction

Among ternary rare-earth transition-metal antimonides R–M–Sb where M is Zn or Cd, the most widespread phases are RM_{1-x}Sb$_2$ (HfCuSi$_2$-type) and R_6ZnSb$_{15}$ (La$_6$MnSb$_{15}$-type) found for the earlier rare earths, and RM_2Sb$_2$ (CaAl$_2$Si$_2$-type) and R_{14}ZnSb$_{11}$ (Ca$_{14}$AlSb$_{11}$-type) found for the divalent rare earths R = Eu and Yb [1]. Some of the ytterbium-containing compounds, such as Yb$_{14}$ZnSb$_{11}$, have been of particular interest because of the anomalous physical properties that might arise from the occurrence of intermediate or mixed valence of Yb [2,3]. Substitution of Ca for Yb has led to solid solutions Ca$_x$Yb$_{1-x}$Zn$_2$Sb$_2$ that may be promising thermoelectric materials [4]. Other new phases recently discovered in the Yb systems include Yb$_9$Zn$_{4+x}$Sb$_9$ [5,6] and Yb$_2$CdSb$_2$ [7].

Investigation of the YbM_2Sb$_2$ (M = Zn, Cd) phases remains incomplete, and some inconsistent results are noted in the literature. For YbZn$_2$Sb$_2$, only cell parameters are known [8,9], the electrical resistivity curve at low temperature (2 to 300 K) [10] is several orders of magnitude greater than that at high temperature (300 to 800 K) [4], and the magnetic properties have been described as either diamagnetic [10] or following Curie-Weiss behaviour [9]. For YbCd$_2$Sb$_2$, a single-crystal structure determination ($R(F)$ = 0.038) has been reported [11], but no electrical or magnetic properties have been measured so far. To resolve some of these ambiguities, we report here a systematic study of these two compounds, including crystal structure determination, electrical and magnetic property measurements, electronic band structure calculations, and X-ray photoelectron spectroscopy.

Experimental

Starting materials were powders of Yb (99.9%, Cerac), Zn (99.9%, Cerac), Cd (99.999%, Cerac), and Sb (99.999%, Alfa-Aesar). Crystals of YbZn$_2$Sb$_2$ and YbCd$_2$Sb$_2$ were originally identified as byproducts in attempts to prepare "Yb$M_{0.7}$Sb$_2$" (in analogy to other RM_{1-x}Sb$_2$ phases) [12,13] by reaction of the elements in evacuated fused-silica tubes heated at 1050 °C for 3 d, followed by slow cooling to 600 °C over 8 d, annealing at 600 °C for 8 d, and quenching in water. The compounds were subsequently prepared in quantitative yield by reaction of the elements, in the correct stoichiometry, placed in alumina crucibles jacketed by outer fused-silica tubes, heated at 1000–1050 °C for 1 d followed by slow cooling to 800–850 °C over 4 d and then to 600 °C over 2 d. Products were evaluated by powder X-ray diffraction patterns collected on an Inel powder diffractometer equipped with a CPS 120 detector, and by energy-dispersive X-ray (EDX) analysis on a Hitachi S-2700 scanning electron microscope.

Single-crystal intensity data for YbZn$_2$Sb$_2$ and YbCd$_2$Sb$_2$ were collected on a Bruker Platform / SMART 1000 CCD diffractometer at 22 °C using

Table 1 Crystallographic data for YbM_2Sb$_2$ (M = Zn, Cd).

Formula	YbZn$_2$Sb$_2$	YbCd$_2$Sb$_2$
Formula mass (amu)	547.28	641.34
Space group	$P\bar{3}m1$ (No. 164)	$P\bar{3}m1$ (No. 164)
a (Å)	4.4424(6)	4.6512(7)
c (Å)	7.4184(9)	7.5661(11)
V (Å^3)	126.79(3)	141.75(4)
Z	1	1
ρ_{calcd} (g cm^{-3})	7.168	7.513
Crystal dimensions (mm)	$0.24 \times 0.13 \times 0.09$	$0.21 \times 0.12 \times 0.05$
Radiation	Graphite monochromated Mo $K\alpha$, $\lambda = 0.71073$ Å	
μ(Mo $K\alpha$) (mm^{-1})	37.91	32.94
Transmission factors	0.011–0.097	0.035–0.216
2θ limits	$5.50° \leq 2\theta$(Mo $K\alpha$) $\leq 66.02°$	$5.38° \leq 2\theta$(Mo $K\alpha$) $\leq 60.78°$
Data collected	$-6 \leq h, k \leq 6; -11 \leq l \leq 11$	$-6 \leq h, k \leq 6; -10 \leq l \leq 10$
No. of data collected	1671 ($R_{int} = 0.046$)	1663 ($R_{int} = 0.042$)
No. of unique data	219 (214 with $F^2 > 2\sigma(F^2)$)	200 (198 with $F^2 > 2\sigma(F^2)$)
No. of variables	10	10
$R(F)$ ($F^2 > 2\sigma(F^2)$) [a]	0.023	0.026
$R_w(F^2)$ [b]	0.056	0.061
Goodness of fit	1.168	1.302
$(\Delta\rho)_{max}, (\Delta\rho)_{min}$ (e Å^{-3})	3.06, −1.06	1.67, −3.00

[a] $R(F) = \sum \left| |F_o| - |F_c| \right| / \sum |F_o|$.

[b] $R_w(F_o^2) = \left[\sum \left[w(F_o^2 - F_c^2)^2 \right] / \sum w F_o^4 \right]^{1/2}$, $w^{-1} = \left[\sigma^2(F_o^2) + (Ap)^2 + Bp \right]$ where $p = \left| max(F_o^2, 0) + 2F_c^2 \right| / 3$.

Table 2 Positional and equivalent isotropic displacement parameters (Å^2) [a] for YbM_2Sb$_2$ (M = Zn, Cd).

	YbZn$_2$Sb$_2$	YbCd$_2$Sb$_2$
Yb in $1a$ (0, 0, 0)		
U_{eq}	0.0144(2)	0.0174(2)
M in $2d$ (⅓, ⅔, z)		
z	0.63267(15)	0.63064(11)
U_{eq}	0.0176(3)	0.0195(3)
Sb in $2d$ (⅓, ⅔, z)		
z	0.25640(6)	0.23749(9)
U_{eq}	0.0121(2)	0.0145(3)

[a] U_{eq} is defined as one-third of the trace of the orthogonalized U_{ij} tensor.

ω scans. Calculations were carried out with use of the SHELXTL (version 6.12) package [14]. Face-indexed numerical absorption corrections were applied. The centrosymmetric space group $P\bar{3}m1$ was chosen and initial atomic positions were located by direct methods, confirming the expected CaAl$_2$Si$_2$-type structure [15]. The crystal structures were refined by full-matrix least-squares methods on F^2 with anisotropic displacement parameters. Table 1 summarizes crystallographic data, Table 2 lists the final values of the atomic positions and displacement parameters, and Table 3 lists selected interatomic distances. Further data, in CIF format, have been sent to Fachinformationszentrum Karlsruhe, Abt. PROKA, 76344 Eggenstein-Leopoldshafen, Germany, as supplementary material No. CSD-419689 and 419690 and can be obtained by contacting FIZ (quoting the article details and the corresponding CSD numbers).

Silver plate-shaped crystals of YbZn$_2$Sb$_2$ and YbCd$_2$Sb$_2$ were selected for electrical resistivity measurements after their identities were confirmed by EDX analysis. The electrical resistivity within the *ab* plane was measured by standard four-probe techniques on a Quantum Design Physical Property Measurement System (PPMS) equipped with an ac transport controller (Model 7100). The current was 100 μA and the frequency was 16 Hz. Measurements of dc magnetic susceptibility were made on ground samples (20–30 mg) between 2 and 300 K on a Quantum Design 9T–PPMS dc magnetometer / ac susceptometer. Susceptibility values were corrected for contributions from the holder and the underlying sample diamagnetism.

Tight-binding linear muffin tin orbital (TB-LMTO) band structure calculations were performed on YbZn$_2$Sb$_2$ within the local density and atomic

Table 3 Selected interatomic distances (Å) and angles (°) in YbM_2Sb$_2$ (M = Zn, Cd).

	YbZn$_2$Sb$_2$	YbCd$_2$Sb$_2$
Yb–Sb (×6)	3.1931(4)	3.2311(5)
Yb–M (×6)	3.7422(9)	3.8757(7)
M–M (×3)	3.2231(14)	3.3346(11)
M–Sb (×3)	2.6936(5)	2.8647(5)
M–Sb	2.7914(13)	2.9747(11)
Sb–M–Sb (×3)	111.10(2)	110.38(2)
Sb–M–Sb (×3)	107.79(2)	108.55(2)

spheres approximations using the Stuttgart TB-LMTO program [16]. The basis sets consisted of Yb 6s/6p/5d/4f, Zn 4s/4p/3d, and Sb 5s/5p/5d/4f orbitals, with the Yb 6p and Sb 5d/4f orbitals being downfolded. Integrations in reciprocal space were carried out with an improved tetrahedron method over 131 independent *k* points.

The valence band spectrum of YbZn$_2$Sb$_2$ was collected on a Kratos AXIS Ultra spectrometer equipped with a monochromatic Al *K*α X-ray source. The pressures throughout the analysis chamber were 10^{-6}–10^{-7} Pa. The resolution function for this instrument has been determined to be 0.4 eV by analysis of the cobalt Fermi edge. Powders of YbZn$_2$Sb$_2$ were pressed onto C tape in air and transferred into the vacuum chamber of the instrument where they were sputter-cleaned with an Ar$^+$ ion beam (4 kV, 10 mA) to remove any surface oxide or contaminates formed. The valence band spectrum was collected using a pass energy of 20 eV and a step size of 0.05 eV. Sample charging was corrected for by calibrating the adventitious C 1s peak to the accepted value of 284.8 eV. The spectrum was analysed with use of the CasaXPS software package [17].

Results and discussion

YbM_2Sb$_2$ (M = Zn, Cd) adopts the trigonal CaAl$_2$Si$_2$-type structure [15], with cell parameters (Table 1) in good agreement with those previously reported (*a* = 4.444(1) Å, *c* = 7.424(1) Å for YbZn$_2$Sb$_2$ [8]; *a* = 4.650(1) Å, *c* = 7.565(2) Å for YbCd$_2$Sb$_2$ [11]). The structure is built up by stacking [M_2Sb$_2$] double layers of edge-sharing MSb$_4$ tetrahedra along the *c* axis, separated by hexagonal nets of Yb atoms that are octahedrally coordinated by Sb atoms (Fig. 1). Consistent with the larger size of Cd relative to Zn, there is an expansion of the structure on going from YbZn$_2$Sb$_2$ to YbCd$_2$Sb$_2$, as manifested by the ~0.2 Å increase in the M–Sb distances within the MSb$_4$ tetrahedra. The ~3.2 Å Yb–Sb distances in YbM_2Sb$_2$ are within the range found in YbSb$_2$ (3.19(1)–3.57(1) Å) [18] which contains divalent Yb, but longer than that found in YbSb (3.041 Å) [19] which contains trivalent Yb. If divalent Yb is assumed, the electron-precise formulation Yb^{2+}(M^{2+})$_2$(Sb^{3-})$_2$ indicates that the Zintl concept is satisfied.
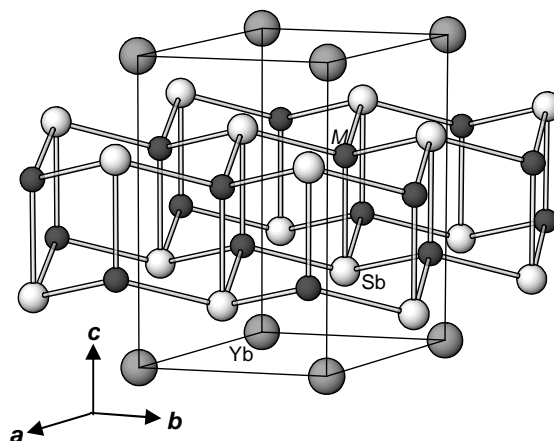

Fig. 1 Structure of YbM_2Sb$_2$ (M = Zn, Cd). The large lightly shaded circles are Yb atoms, the small solid circles are M atoms, and the medium open circles are Sb atoms.

The electrical resistivity profile from 2 to 300 K for YbZn$_2$Sb$_2$ suggests a small band gap semiconductor or a semimetal (Fig. 2a). The absolute resistivity at room temperature is high (ρ_{300} = 0.53 mΩ·cm), similar to that found in a previous measurement from 300 to 800 K (ρ_{300} = 0.32 mΩ·cm) [4] but in considerable disagreement with another measurement from 5 to 300 K (ρ_{300} = 0.25 Ω·cm) [10] (note the difference in units). Moreover, the temperature coefficient found here is essentially identical to that in the previous high-temperature measurement (dρ/d*T* = 0.0012 mΩ·cm/K) [4]. In contrast, the resistivity for YbCd$_2$Sb$_2$ is substantially higher, with ρ_{300} = 50 mΩ·cm, and exhibits a characteristic minimum near 80 K suggestive of Kondo lattice behaviour in which dilute magnetic impurities cause scattering of conducting electrons at low temperatures (Fig. 2b). Because the resistivity measurements were performed on discrete single crystals, this observation suggests the presence of some trivalent Yb that is intrinsic to YbCd$_2$Sb$_2$.

The magnetic susceptibility reveals nearly temperature-independent paramagnetism throughout most of the temperature range superimposed with a Curie tail at low temperatures (Fig. 3). For YbZn$_2$Sb$_2$, these results agree qualitatively with the paramagnetism (μ_{eff} = 2.38 μ_B, θ_p = –108 K) reported
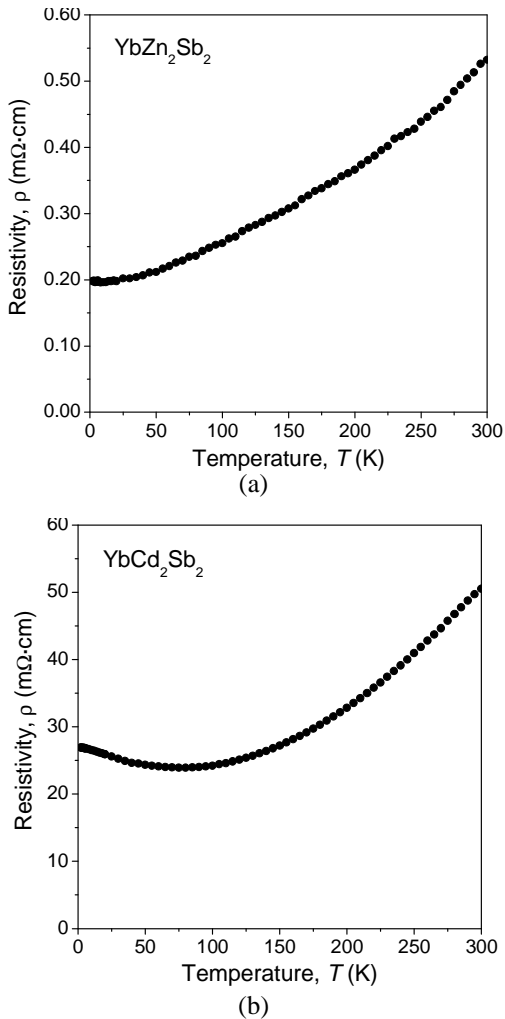
Fig. 2 Electrical resistivity of single crystals of (a) YbZn$_2$Sb$_2$ and (b) YbCd$_2$Sb$_2$ measured within the *ab* plane.
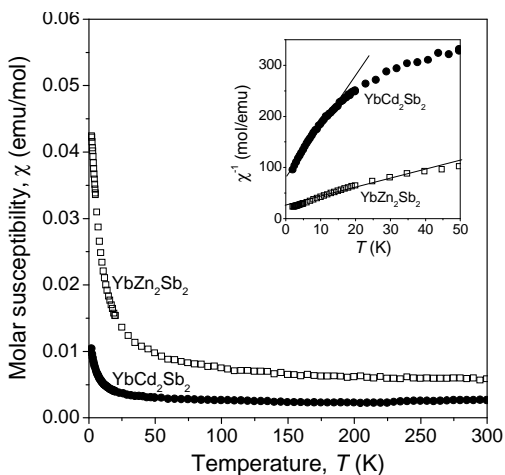

Fig. 3 Magnetic susceptibility of YbZn$_2$Sb$_2$ (open squares) and YbCd$_2$Sb$_2$ (solid circles). The inset shows fits of the inverse susceptibility to the Curie-Weiss law at low temperature.

by Zwiener *et al.* from 80 to 290 K [9], but differ from the large diamagnetic response seen at all temperatures by Pfleiderer *et al.* [10], who also reported the inconsistently high resistivity described above. Fitting of the low-temperature portion of the inverse susceptibility to the Curie-Weiss law gives μ_{eff} = 2.1 μ_B for YbZn$_2$Sb$_2$ and 0.9 μ_B for YbCd$_2$Sb$_2$. Given that the theoretical magnetic moments are 0 μ_B for Yb^{2+} (4f^{14}) and 4.5 μ_B for Yb^{3+} (4f^{13}), the observed nonzero moments suggest the presence of some trivalent Yb. For comparison, YbZn$_2$As$_2$ also exhibits a nonzero magnetic moment of 2.3 μ_B/Yb [20]. It is customary to dismiss a small nonzero moment in divalent Yb compounds to minor amounts of impurities such as Yb$_2$O$_3$. However, the resistivity minimum seen earlier provides evidence that a small amount of trivalent Yb may be intrinsic, on the order of ~20% in YbZn$_2$Sb$_2$ and ~4% in YbCd$_2$Sb$_2$, if the nonzero moment is attributed entirely to these compounds and not to another unidentified impurity. Overall, our observations tend to support the earlier proposal that YbZn$_2$Sb$_2$ exhibits an intermediate Yb valence [9].

The calculated band structure shows that the Fermi level (E_f) falls at a pseudogap with a low density of states (DOS) (Fig. 4a). The filled bands below E_f are predominantly derived by mixing of Zn 3d and Sb 5p states, leading to essentially optimized Zn–Sb bonding interactions, as revealed by the crystal orbital Hamiltonian population (COHP) curve (Fig. 4b). The sharp peak just below E_f represents filled Yb 4f states that are highly localized, consistent with the presence of Yb^{2+} as predicted by the Zintl formalism. However, this peak is merely 0.2 eV below E_f, and the Zn and Sb projections of the DOS reveal that a small hybridization with the Yb 4f states is possible, which may account for the nonzero magnetic moment observed in YbZn$_2$Sb$_2$.

The experimental valence band spectrum of YbZn$_2$Sb$_2$ (Fig. 5) agrees qualitatively with the calculated band structure but is complicated by additional multiplet features. The sharp Yb 4f$_{7/2}$ and 4f$_{5/2}$ doublet at the Fermi edge is characteristic of divalent Yb, but there is also a broad multiplet structure at higher binding energy centred at ~8 eV that suggests the presence of some trivalent Yb [3]. As with the magnetic data, it is difficult to completely rule out the occurrence of slight surface oxidation leading to formation of small amounts of Yb$_2$O$_3$; however, this would only contribute a small amount to the spectrum because the surface was sputter-cleaned prior to analysis. As shown in Fig. 5, an intense Zn 3d peak is observed near 10 eV, in agreement with previous spectra of Zn-containing materials [21]. Located beneath the Zn and Yb peaks are the Sb 5p and 5s states, which are difficult to observe because of their lower photoelectron cross-sections relative to those of the Yb 4f states [22].

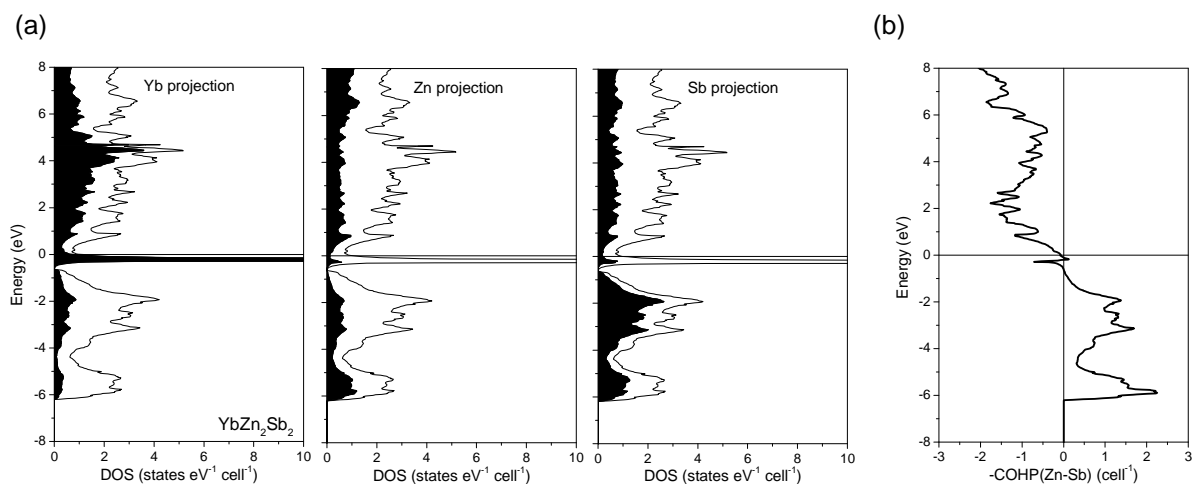On balance, the results presented here provide evidence in favour of the occurrence of a mixed or

Fig. 4 (a) Total density of states (DOS) for YbZn$_2$Sb$_2$ and its Yb, Zn, and Sb projections. The Fermi level is marked by a horizontal line at 0 eV. (b) Crystal orbital Hamilton population (COHP) curve for Zn–Sb contacts in YbZn$_2$Sb$_2$.
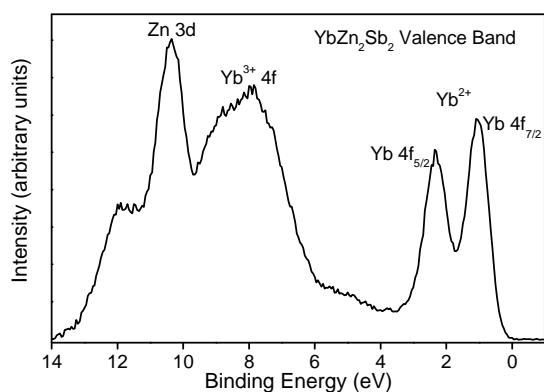

Fig. 5 Valence band spectrum of YbZn$_2$Sb$_2$.

intermediate valence of Yb in these compounds, and provide impetus for further study of other ternary ytterbium antimonides.

References

[1] O.L. Sologub, P.S. Salamakha, in: K.A. Gschneidner Jr., J.-C.G. Bünzli, V.K. Pecharsky (Eds.), *Handbook on the Physics and Chemistry of Rare Earths*, Vol. 33, Elsevier, Amsterdam, 2003, pp. 35–146.

[2] I.R. Fisher, S.L. Bud'ko, C. Song, P.C. Canfield, T.C. Ozawa, S.M. Kauzlarich, *Phys. Rev. Lett.* 85 (2000) 1120–1123.

[3] A.P. Holm, T.C. Ozawa, S.M. Kauzlarich, S.A. Morton, G.D. Waddill, J.G. Tobin, *J. Solid State Chem.* 178 (2005) 262–269.

[4] F. Gascoin, S. Ottensmann, D. Stark, S.M. Haïle, G.J. Snyder, *Adv. Funct. Mater.* 15 (2005) 1860–1864.

[5] S. Bobev, J.D. Thompson, J.L. Sarrao, M.M. Olmstead, H. Hope, S.M. Kauzlarich, *Inorg. Chem.* 43 (2004) 5044–5052.

[6] S.-Q. Xia, S. Bobev, *J. Am. Chem. Soc.* 129 (2007) 10011–10018.

[7] S.-Q. Xia, S. Bobev, *J. Am. Chem. Soc.* 129 (2007) 4049–4057.

[8] P. Klüfers, H. Neumann, A. Mewis, H.-U. Schuster, *Z. Naturforsch.* 35B (1981) 1317–1318.

[9] G. Zwiener, H. Neumann, H.-U. Schuster, *Z. Naturforsch.* 86B (1981) 1195–1197.

[10] C. Pfleiderer, R. Vollmer, M. Uhlarz, A. Faisst, H. von Löhneysen, A. Nateprov, *Physica B* 312–313 (2002) 352–353.

[11] A. Artmann, A. Mewis, M. Roepke, G. Michels, *Z. Anorg. Allg. Chem.* 622 (1996) 679–682.

[12] O.Ya. Zelinska, A. Mar, *J. Solid State Chem.* 179 (2006) 3776–3783.

[13] A.V. Tkachuk, O.Ya. Zelinska, A. Mar, *J. Solid State Chem.* 179 (2006) 1506–1512.

[14] G.M. Sheldrick, *SHELXTL, Version 6.12*, Bruker AXS Inc., Madison, WI, 2001.

[15] E.I. Gladyshevskii, P.I. Kripyakevich, O.I. Bodak, *Ukr. Fiz. Zh.* 12 (1967) 447–452.

[16] R. Tank, O. Jepsen, A. Burkhardt, O.K. Andersen, *TB-LMTO-ASA Program, Version 4.7*, Max Planck Institut für Festkörperforschung, Stuttgart, 1998.

[17] N. Fairley, *CasaXPS, Version 2.3.9*, Casa Software Ltd., Teighnmouth, Devon, UK, 2003 (www.casaxps.com).

[18] R. Wang, R. Bodnar, H. Steinfink, *Inorg. Chem.* 5 (1966) 1468–1470.

[19] R.E. Bodnar, H. Steinfink, *Inorg. Chem.* 6 (1967) 327–330.

[20] A. Nateprov, J. Cisowski, J. Heimann, I. Mirebeau, *J. Alloys Compd.* 290 (1999) 6–9.

[21] G.W. Cong, W.Q. Peng, H.Y. Wei, X.X. Han, J.J. Wu, X.L. Liu, Q.S. Zhu, Z.G. Wang, J.G. Lu, Z.Z. Ye, L.P. Zhu, H.J. Qian, R. Su, C.H. Hong, J. Zhong, K. Ibrahim, T.D. Hu, *Appl. Phys. Lett.* 88 (2006) 062110-1–062110-3.

[22] J.H. Scofield, *J. Electron Spectrosc. Relat. Phenom.* 8 (1976) 129–137.